A handheld laser scanning confocal reflectance imaging–confocal Raman microspectroscopy system

Chetan A. Patil,[1] Christopher L. Arrasmith,[2] Mark A. Mackanos,[1] David L. Dickensheets,[2] and Anita Mahadevan-Jansen[1,*]

[1]*Department of Biomedical Engineering, Station B, Box 351631, Vanderbilt University, Nashville TN, 37235, USA*
[2]*Department of Electrical and Computer Engineering, Montana State University, 610 Cobleigh Hall, Bozeman, MT, 59717, USA*
*anita.mahadevan-jansen@vanderbilt.edu

Abstract: Confocal reflectance microscopy and confocal Raman spectroscopy have shown potential for non-destructive analysis of samples at micron-scale resolutions. Current studies utilizing these techniques often employ large bench-top microscopes, and are not suited for use outside of laboratory settings. We have developed a microscope which combines laser scanning confocal reflectance imaging and confocal Raman spectroscopy into a compact handheld probe that is capable of high-resolution imaging and spectroscopy in a variety of settings. The compact size of the probe is largely due to the use of a MEMS mirror for beam scanning. The probe is capable of axial resolutions of up to 4 μm for the confocal imaging channel and 10 μm for the confocal Raman spectroscopy channel. Here, we report instrument design, characterize optical performance, and provide images and spectra from normal skin to demonstrate the instrument's capabilities for clinical diagnostics.

OCIS codes: (170.3890) Medical optics instrumentation; (170.1790) Confocal microscopy; (170.5660) Raman spectroscopy; (170.1610) Clinical applications; (170.1870) Dermatology; (170.6935) Tissue characterization.

References and links

1. D. B. Hovis and A. H. Heuer, "The use of laser scanning confocal microscopy (LSCM) in materials science," J. Microsc. **240**(3), 173–180 (2010).
2. A. Gupper, P. Wilhelm, M. Schmied, S. G. Kazarian, K. L. A. Chan, and J. Reußner, "Combined application of imaging methods for the characterization of a polymer blend," Appl. Spectrosc. **56**(12), 1515–1523 (2002).
3. J. T. Fredrich, "3D imaging of porous media using laser scanning confocal microscopy with application to microscale transport processes," Phys. Chem. Earth, Part A Solid Earth Geod. **24**(7), 551–561 (1999).
4. K. D. McKeegan, A. B. Kudryavtsev, and J. W. Schopf, "Raman and ion microscopic imagery of graphitic inclusions in apatite from older than 3830 Ma Akilia supracrustal rocks, west Greenland," Geology **35**(7), 591–594 (2007).
5. M. Claybourn and M. Ansell, "Using Raman spectroscopy to solve crime: inks, questioned documents and fraud," Sci. Justice **40**(4), 261–271 (2000).
6. R. S. Scott, P. S. Ungar, T. S. Bergstrom, C. A. Brown, F. E. Grine, M. F. Teaford, and A. Walker, "Dental microwear texture analysis shows within-species diet variability in fossil hominins," Nature **436**(7051), 693–695 (2005).
7. M. A. Pabst, I. Letofsky-Papst, M. Moser, K. Spindler, E. Bock, P. Wilhelm, M. D. Leopold Dorfer, J. B. Geigl, M. Auer, M. R. Speicher, and F. Hofer, "Different staining substances were used in decorative and therapeutic tattoos in a 1000-year-old Peruvian mummy," J. Archaeol. Sci. **37**(12), 3256–3262 (2010).
8. K.-J. Halbhuber and K. König, "Modern laser scanning microscopy in biology, biotechnology and medicine," Ann. Anat. **185**(1), 1–20 (2003).
9. R. Petry, M. Schmitt, and J. Popp, "Raman spectroscopy--a prospective tool in the life sciences," ChemPhysChem **4**(1), 14–30 (2003).
10. P. J. Caspers, G. W. Lucassen, and G. J. Puppels, "Combined in vivo confocal Raman spectroscopy and confocal microscopy of human skin," Biophys. J. **85**(1), 572–580 (2003).
11. C. L. Arrasmith, D. L. Dickensheets, and A. Mahadevan-Jansen, "MEMS-based handheld confocal microscope for in-vivo skin imaging," Opt. Express **18**(4), 3805–3819 (2010).

12. M. Rajadhyaksha, R. R. Anderson, and R. H. Webb, "Video-rate confocal scanning laser microscope for imaging human tissues in vivo," Appl. Opt. **38**(10), 2105–2115 (1999).
13. P. J. Caspers, G. W. Lucassen, R. Wolthuis, H. A. Bruining, and G. J. Puppels, "In vitro and in vivo Raman spectroscopy of human skin," Biospectroscopy **4**(S5), S31–S39 (1998).
14. A. Palm, "Raman spectrum of polystyrene," J. Phys. Chem. **55**(8), 1320–1324 (1951).
15. C. A. Lieber and A. Mahadevan-Jansen, "Automated method for subtraction of fluorescence from biological Raman spectra," Appl. Spectrosc. **57**(11), 1363–1367 (2003).
16. P. J. Caspers, G. W. Lucassen, E. A. Carter, H. A. Bruining, and G. J. Puppels, "In vivo confocal Raman microspectroscopy of the skin: noninvasive determination of molecular concentration profiles," J. Invest. Dermatol. **116**(3), 434–442 (2001).
17. A. Nijssen, T. C. Bakker Schut, F. Heule, P. J. Caspers, D. P. Hayes, M. H. A. Neumann, and G. J. Puppels, "Discriminating basal cell carcinoma from its surrounding tissue by Raman spectroscopy," J. Invest. Dermatol. **119**(1), 64–69 (2002).
18. C. A. Lieber, S. K. Majumder, D. L. Ellis, D. D. Billheimer, and A. Mahadevan-Jansen, "In vivo nonmelanoma skin cancer diagnosis using Raman microspectroscopy," Lasers Surg. Med. **40**(7), 461–467 (2008).
19. M. Rajadhyaksha, S. González, J. M. Zavislan, R. R. Anderson, and R. H. Webb, "In vivo confocal scanning laser microscopy of human skin II: advances in instrumentation and comparison with histology," J. Invest. Dermatol. **113**(3), 293–303 (1999).
20. M. Rajadhyaksha, G. Menaker, T. Flotte, P. J. Dwyer, and S. González, "Confocal examination of nonmelanoma cancers in thick skin excisions to potentially guide mohs micrographic surgery without frozen histopathology," J. Invest. Dermatol. **117**(5), 1137–1143 (2001).

1. Introduction

Laser-scanning confocal reflectance microscopy (CM) and confocal Raman spectroscopy (CRS) are powerful tools for non-destructive analysis that produce inherently complementary data sets. Scanning confocal microscopy is capable of subsurface imaging of microstructure in real-time, however the information contained within the reflectance images does not directly identify the specific compositional properties. CRS, on the other hand, can relate intrinsic compositional properties without the need for exogenous dyes, however image formation can be time consuming due to the fundamentally weak nature of Raman scattering. The two techniques have demonstrated a diverse range of applications that include materials and polymer science [1,2], geology and environmental sciences [3,4], forensics [5], anthropology and archaeology [6,7], and bioscience and medical diagnostics [8,9].

In many instances, collecting information related to both microstructure and molecular composition would be advantageous for more thorough sample characterization. Often, this requires separate benchtop instruments, which can reduce ease of use and the accuracy of data registration. The promise of highly specific biochemical analysis of microstructural features has motivated prior work in the development of a dual-modal CM-CRS instrument [10]. This device was used to demonstrate the value of dual-modal reflectance microscopy - Raman spectroscopy in the skin. There are applications, however, where it can be difficult to bring the sample to the microscope and orient it to suit the microscope's design. A compact dual-mode instrument with the flexibility to make well-correlated chemical and structural measurements away from the benchtop would further simplify sample analysis.

In this paper we describe a handheld instrument that combines confocal reflectance microscopy and confocal Raman spectroscopy for measurement of highly scattering samples. The instrument may be configured to accommodate different imaging field sizes and resolutions. The primary design objective was to reduce the experimental constraints of a benchtop CM-CRS system. The instrument we describe here was developed on the platform of a recently reported MEMS based handheld scanning confocal microscope [11]. The use of a MEMS scanner enabled the probe to be small enough to easily hold by hand and image at 56 frames/sec. This paper presents the design, characterization, and demonstration of a dual-modal probe that integrates CRS into the handheld CM platform. A detailed description of the design and characterization of the stand-alone CM sub-system can be found elsewhere [11]. This paper emphasizes characterization of the CRS collection parameters in relation to CM, registration of the two modalities, and initial demonstrations of measurements in the skin.

2. Microscope design

Both the CM and CRS sub-systems use the same single-mode 830 nm external cavity diode laser in Littrow configuration (Sacher Lasertechnik). The laser source, CM detection, amplification, control electronics, computer, and Raman spectrometer are located on a control station that is separate from the handheld probe portion of the device. This design minimizes the size of the hand-piece, which is tethered to the control station with fiber-optic and electrical connections. The control station is cart mounted and can be operated with a battery pack for mobile operation. The CM optical design uses a polarization-based light-launch/collection configuration that allows a single fiber to be used for illumination and detection [11]. This simplifies the design and alignment of the system and reduces the effect of specular reflections from the optics within the microscope. The linearly-polarized laser is reflected off of a polarizing beam splitter and focused into a single mode PM fiber with a 5.3 μm mode-field diameter which couples the light to the hand piece.
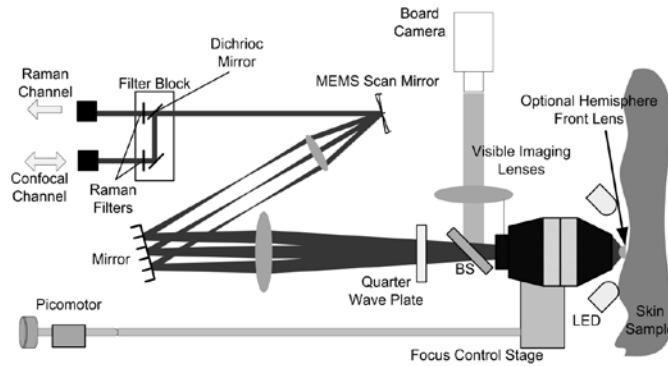
(a)
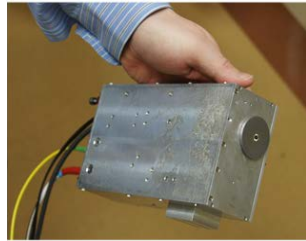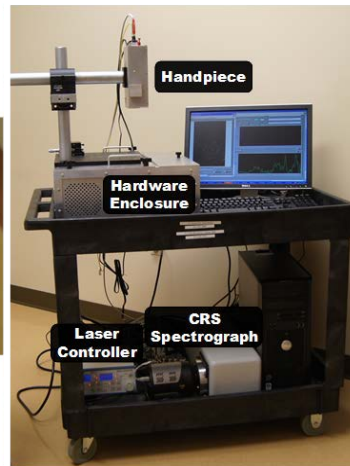
(b)   (c)

Fig. 1. The CM-CRS system. (a) Schematic diagram of the microscope. (b) Photograph of the hand-piece. The overall size of the hand-piece is 7" (L) x 4.5" (W) x 2.25" (H). (c) Photograph of the CM-CRS system. The controls for the MEMS scanner, picomotor, camera, avalanche-photodiode (APD), and electronic gain box for CM, and laser system are within the hardware enclosure, while the laser controller and Raman spectrometer are on the lower shelf of the cart.

Figure 1 contains an illustration of the handheld microscope layout (a), a photograph of the probe(b), and a photograph of the entire system and cart. Upon entering the microscope, the light from the PM fiber is collimated and travels through the filter block containing an

830 nm bandpass filter and a dichroic mirror (Chroma). The dichroic mirror reflects the 830 nm illumination beam towards a MEMS mirror (Microvision, Inc.) which provides the two-dimensional scanning necessary for confocal imaging. A pair of telescope lenses expand the beam with a magnification of 3x to fill the rear pupil of the objective lens, and also images the MEMS scanner onto the back focal plane of the objective lens, which is necessary for telecentric scanning in the object plane. A quarter wave-plate behind the objective lens circularly polarizes the illumination light. The wave plate is placed as close to the sample as possible to minimize artifacts due to reflections from previous optical surfaces, as these reflections will be cross polarized with respect to light scattered from the sample. The beam splitter shown behind the objective lens is used to relay a large area white-light image to the CCD board camera to aid in registration of the microscope image to features of the sample that are superficially visible. White LEDs in front of the objective lens provide illumination for the CCD image. A removable adapter plate on the front of the microscope allows the sample interface to be changed from a clear aperture to a hemisphere front lens, which increases the NA of the microscope as discussed below. Laser light elastically scattered from the sample retraces the illumination path, with a 90° polarization rotation relative to the illumination light due to a second pass through the quarter wave plate, and is coupled into the orthogonal axis of the same PM fiber that delivered the input light. Upon return to the instrument control station, the light reflected from the sample is separated from reflections within the system by a polarization beam splitter, and detected by an Avalanche Photodiode (APD) (Hamamatsu). The Stokes shifted Raman scatter generated within the sample follows the same path back to the filter block where it passes through the dichroic mirror and long pass filter before being fiber coupled ($f_{coupling\ lens} = 4.5$) into a multi-mode, low-OH fiber for delivery to the Raman spectrometer. The spectrometer is made up of an f/1.8 high-throughput spectrograph with an 830 nm transmissive grating (Kaiser Optical Systems), and a deep-depletion, back-illuminated, thermo-electrically cooled CCD (Princeton Instruments) with a spectral resolution of 7 cm^{-1}. A 2D CCD array allows vertical binning of the exposed pixels and enabled investigation of the performance of different sizes of CRS collections fibers. Spectrograph calibration is performed using the atomic emission lines of a Neon-Argon lamp for absolute wavenumber calibration, and an acetaminophen tablet for the relative wavenumber axis. Variations in system response were corrected using a NIST calibrated white light source (Newport Spectra-Physics) and a broadband spectral intensity standard.

The two-dimensional MEMS scan mirror simplifies the design of the confocal microscope compared to the x-y pair of galvanometer scan mirrors that are typically used in scanning microscopes. In the fast scan direction, the mirror operates in a resonant sinusoidal displacement mode with a frequency of 22 kHz. The slow axis is scanned in a saw tooth shaped pattern at 56 Hz, and dictates the maximum 56 Hz frame rate for confocal imaging. HSYNC and VSYNC pulses from the mirror controller allow for image formation using an image acquisition card (National Instruments). The usable aperture of the mirror is 1 mm, which constrains the collimated input beam size.

In order to acquire high-quality images and spectra from highly scattering samples, a high numerical aperture (NA>.55) is necessary [12,13]. The confocal microscope is designed to be used with different objective lenses with different NA's in order to achieve either high magnification or a wider field of view (FOV). Here, we report characterization with two air immersion objective lenses: a Leica 100x 0.75 NA Long Working Distance (LWD) objective (f = 2 mm) and a Nikon 50x 0.55 NA LWD objective (f = 4 mm). The total magnification from the focal plane of the objectives to the illumination/collection fibers is 3.375 for the 50x objective and 6.75 for the 100x objective. This holds for both the CM and CRS optical paths. LWD objectives enable the placement of an optional BK7 hemispherical lens in front of the objective lenses to further increase the NA. Through testing we found that water coupling the hemispherical front lens to the sample in combination with either of the objective lenses produced better results for skin imaging than the objective lens alone [11]. The hemisphere is mounted in a round stainless steel front piece, as seen in Fig. 1(b). The improved imaging is

partially due to an increase in NA from the hemisphere, but also partially due to specific to the challenge of *in vivo* skin imaging, where the flat front surface of the hemisphere provides a rigid plane to stabilize bulk movement of the sample. When used with the hemisphere lens the 100x objective provides a 260 x 198 µm FOV, while the FOV using the 50x objective is 520 x 396 µm. It is important to note that the expanded FOV comes at the cost of reduced resolution and cross sectioning ability. The measured illumination power at the sample with the 50x objective is 12.0 mW with and 14.3 mW without the hemisphere. With the 100x objective, the laser power is 8.9 mW with and 9.7 mW without the hemisphere. In order to acquire measurements from a variety of depths, the objective is mounted to a focus control stage that is driven by a piezo-electric picomotor (New Focus). The picomotor allows high-resolution movement of the objective stage and can be calibrated to approximate measurement depth.

Initial alignment of the microscope to superficially visible features of interest can be performed by fixing the front piece to the sample at the desired measurement location with two-sided tape prior to attachment of the microscope body. When the body of the microscope is brought into position and aligned with the front-piece, a set of magnets on the front-piece and microscope bring the two firmly together, and a set of three steel bearings ensure centering and consistent placement of the front piece on the microscope.

3. Optical performance

The performance of the CRS sub-system with respect to detected signal intensity and axial resolution is characterized as a function of detection fiber size in order to identify the preferred fiber for CRS. The performance of the CRS and CM systems was then characterized with respect to the axial response function and the lateral edge response function in order to determine the cross-sectioning capabilities and transverse resolution of the microscope. Finally, registration of the CRS measurement position to the CM image was verified in an optical phantom.

3.1. CRS detection fiber size

In fiber-based microscopes, there is a well-known tradeoff between detected signal intensity and axial resolution that is a function of the size of the detection fiber. Close attention to this tradeoff is critical in CRS due to the relatively weak nature of inelastic scattering. This is particularly true when the instrument is designed for an application where priority is placed on short spectral acquisition times, such as clinical diagnostics. In order to examine the effect of the detection fiber size on the CRS sub-system, measurements of the axial response

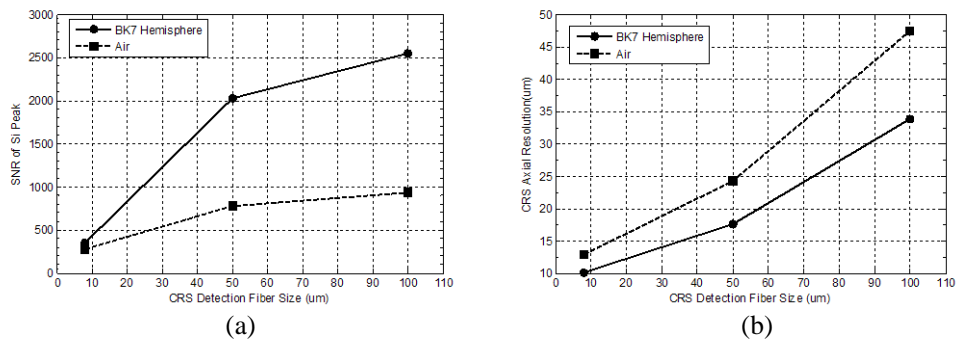(a)   (b)

Fig. 2. Effect of CRS detection fiber size on SNR and axial resolution. Measurements of SNR and axial resolution were made using a polished Si substrate, and evaluating the intensity of the 520 cm^{-1} peak. The plot of SNR vs. detection fiber size (a) shows a sharp improvement when going from an 8 µm detection fiber to a 50 µm fiber. The plot of axial resolution vs. detection fiber size (b) shows the degradation in axial resolution with increasing fiber size. Both (a) and (b) demonstrate the performance improvements offered by the BK7 hemisphere. All measurements were made using the 50x objective lens.

function and signal-to-noise ratio (SNR) were made with detection fibers having 8 μm, 50 μm, and 100 μm core sizes.

The axial response function was measured by placing a polished silicon substrate at the front of the microscope, translating through the focus, and recording the intensity of the 520 cm^{-1} silicon peak as a function of displacement. The translation step size varied from 2 to 5 μm based on the width of the response function. The axial resolution was then defined as the full-width-at-half-max (FWHM) of the best Gaussian fit of the axial response function. The SNR was defined as the ratio of the intensity of the silicon peak at the axial response maxima divided by the standard deviation of the adjacent spectral band from 600 to 700 cm^{-1}, which does not contain any Raman signatures. Measurements were made using the 50x objective both with and without the hemisphere. The spectral acquisition time for measurements was fixed at 0.2 sec.

Plots of SNR and axial resolution as a function of CM detection fiber size can be seen in Figs. 2 (a) and (b), respectively. As expected, the 8 μm fiber resulted in the lowest signal-to-noise ratio (345 with the water coupled hemisphere, 276 in air), but produced the highest resolution. The 50 μm fiber resulted in a large increase in the SNR, particularly with the BK7 hemisphere which improved the SNR by a factor of > 5. This SNR increase came at the expense of axial resolution, which in the case of the BK7 hemisphere decreased from 10.0 μm to 17.6 μm. Finally, while the 100 μm fiber resulted in a largest SNR's both with and without the hemisphere, the relative improvement was not as significant as that seen by increasing the detection fiber size from 8 μm to 50 μm. Furthermore, the axial resolution was degraded to > 30 μm, which is a factor of 3 worse than that achieved with the 8 μm detection fiber in combination with the hemisphere.

3.2. Axial response

A critical performance specification in any confocal microscope or spectroscope is the axial resolution. Measurement of the confocal channel axial response was performed by placing a mirror in front of the microscope and recording the intensity with an oscilloscope while translating the objective lens so its focus passed through the location of the mirror. Representative plots of the axial response for both the confocal and Raman channels are shown in Fig. 3. The axial resolution was then defined as the FWHM of the measured axial response. In the CM channel, the output of the APD was recorded as function of mirror displacement at a sufficiently high sampling rate to directly measure the FWHM of the response. In addition, Raman channel measurements were performed as described above. As a result of the lower sampling rate, a Gaussian fit of the peak used to determine the FWHM.

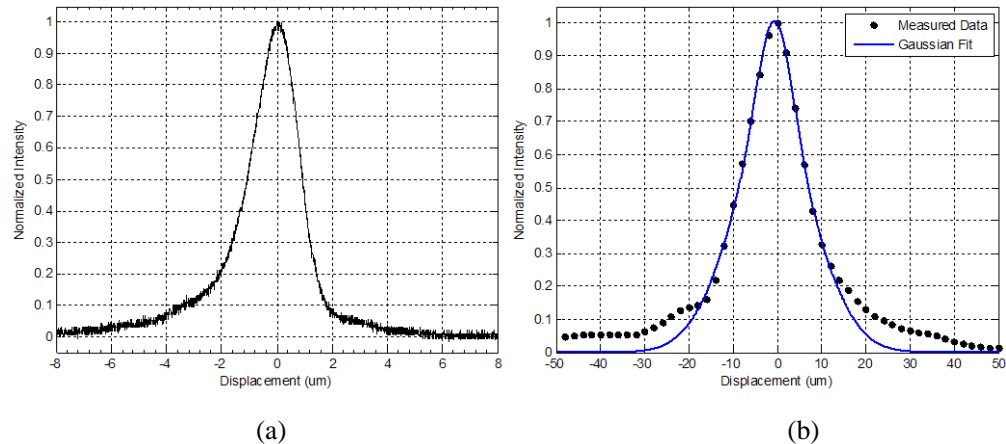(a)   (b)

Fig. 3. Representative axial response functions. Measured LSCM axial response function (a) and the measured CRS axial response (black dots) and Gaussian fit (blue line) (b) for the 100x objective with aperture front piece. CRS was measured using the 50 μm core fiber.

Table 1 lists the axial resolutions of CM and CRS sub-systems as measured using the 100x and 50x objectives, both with and without the hemisphere. Hemisphere measurements were made in a water coupling medium to replicate experimental conditions. As expected, the best resolution was seen with the 100x objective used in conjunction with the hemisphere for both CM (1.5 μm) and CRS (13 μm). All Raman response functions were measured using the 50 μm core collection fiber.

Table 1. Axial resolutions of the confocal channel and Raman channel (50μm core fiber)

Channel	Air (μm)	Hemisphere (μm)
100x confocal channel	2	1.5
50x confocal channel	4.8	3.8
100x Raman channel	18	13
50x Raman channel	24	17

3.3. Edge response and PSF

The edge response of the confocal channel was found by placing a cleaved silicon edge at the focus and perpendicular to the fast scan direction The response was then recorded from the APD during the scan. Raman channel edge measurements were made by mounting the silicon to a differential micrometer driven translation stage. Raman spectra were collected while translating the edge laterally across the focus in 0.25 μm steps. Figure 4 shows representative edge response functions for the confocal and Raman channels.

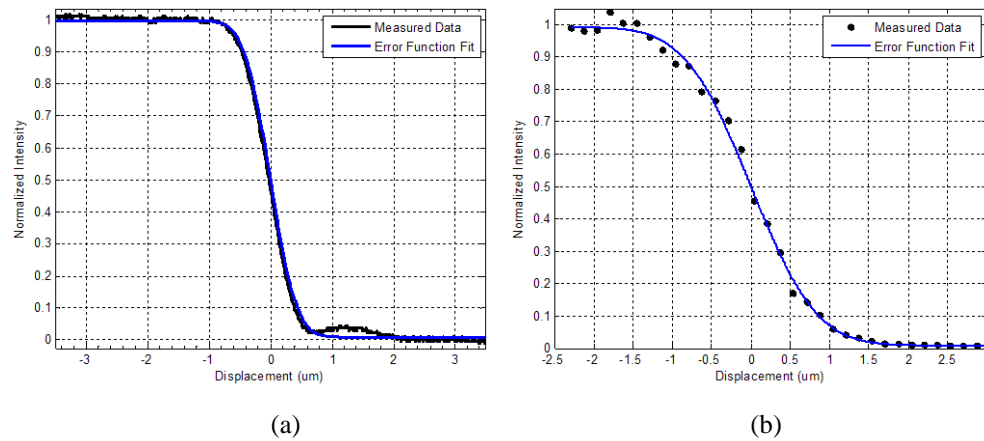(a)   (b)

Fig. 4. Representative edge response functions for the 50x objective with the hemisphere front-piece. Measured data (black line) and fit for the CM channel (a). Measured data and fit for the CRS channel (b). Data is fit to the error function.

An error function was fit to the edge response data, and the transverse resolution was then defined as the FWHM of the Gaussian profile calculated by taking the derivative of the fitted function. The FWHM calculations derived from the edge response data for the different configurations can be seen in Table 2. These figures show single-micron scale resolution for all instances.

Table 2. Transverse resolution of the confocal and Raman channel (50μm core fiber)

Channel	Air (μm)	Hemisphere (μm)
100x confocal channel	0.47	0.37
50x confocal channel	0.74	0.60
100x Raman channel	1.08	0.73
50x Raman channel	1.45	1.15

3.4. Registration of Raman measurement position within CM image plane

All Raman spectra were acquired from a fixed point along the central optical axis of the objective with the MEMS scanner turned off. Acquisition of spectra along the central axis

was necessary in order to avoid off-axis degradation of CRS performance. In order to register the CRS measurement position within the CM image plane, an optical phantom was created using 5 µm polystyrene beads fixed in gelatin. The gelatin phantom was translated laterally with the confocal imaging turned off until a Raman signature from one of the beads was seen. Confocal imaging was then enabled, and the location of the bead was marked on the image with crosshairs (Figs. 5(a,c)). This co-registration was then iteratively fine-tuned to ensure a registration error of 5 µm or less. Co-registration of CM and CRS was verified by acquiring a Raman spectrum after translating the optical phantom a few microns away to an area without any microspheres (Figs. 5(b,c)). Co-registration ensured well correlated confocal images and Raman spectra.
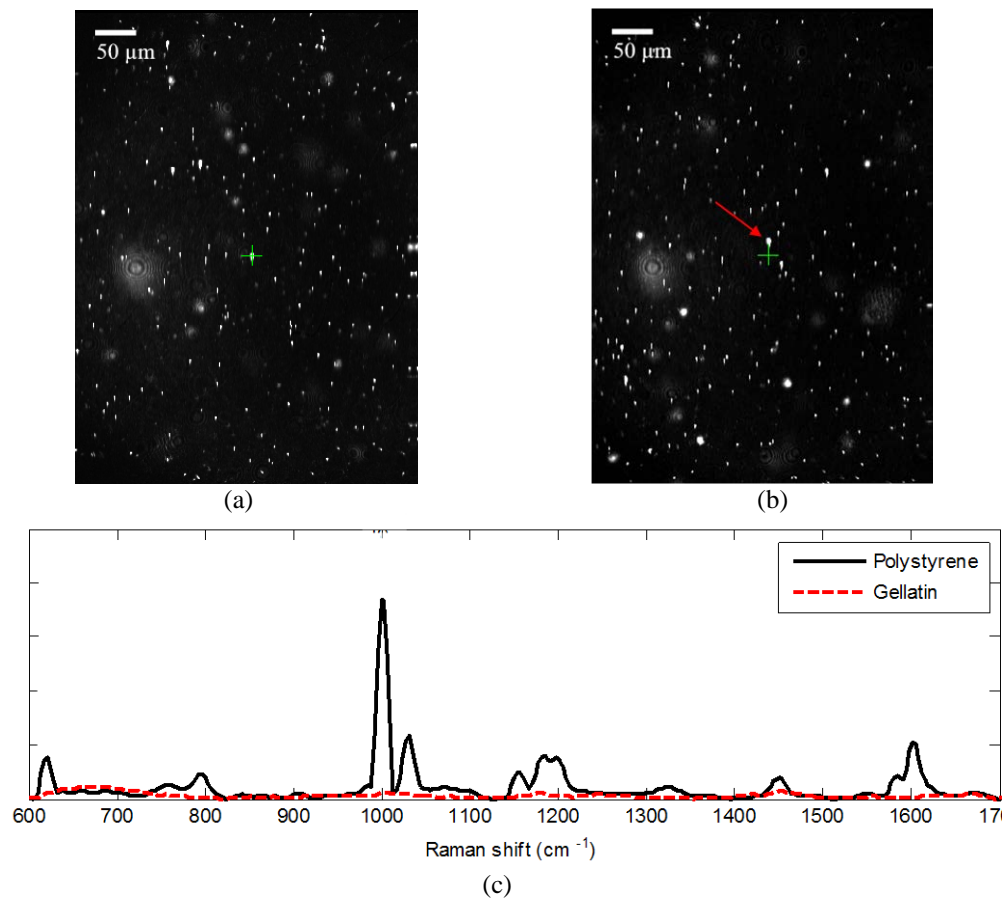

(a)   (b)

(c)

Fig. 5. Co-registration of Raman sampling location and confocal imaging was done using 5 µm polystyrene microspheres in gelatin solution. Crosshairs mark the Raman sampling location. On (a) and off (b) the microsphere shows distinction in Raman spectra (c), where the spectra corresponding to (a) is shown as the solid black line, and the spectra corresponding to (b) is shown as the dashed red line. The spectrum acquired on the bead clearly shows the characteristic spectral features of polystyrene, including the prominent peaks at 628, 1011, 1034, and 1613 cm^{-1} [14]. Image dimensions in (a) and (b) is 520 x 396 µm.

4. Results

In order to demonstrate the capabilities of the microscope system and handheld probe, measurements were taken of skin, *in vivo*.

4.1. Comparison of 50x and 100x objective lenses in tissue

Sub-micron lateral resolution combined with an axial resolution under 5 µm allows the confocal imaging channel to discern detail within individual skin cells. Figures 6 (a,b) show a comparison of the CM images acquired with the 100x and 50x objective lenses from a depth of approximately 20 µm in the stratum spinosum of the back palm. Cell membranes and nuclei are clearly visible with the 100x objective in Fig. 6 (a). The reduced resolution of the 50x objective decreases the visibility of nuclei, while still clearly depicting the cell membranes (Fig. 6 (b)). Corresponding CRS measurements acquired at similar depths are seen in Figs. 6 (c,d). Both spectra were acquired with 30 second acquisition times. The spectra were then processed using a modified polynomial fitting routine to remove tissue
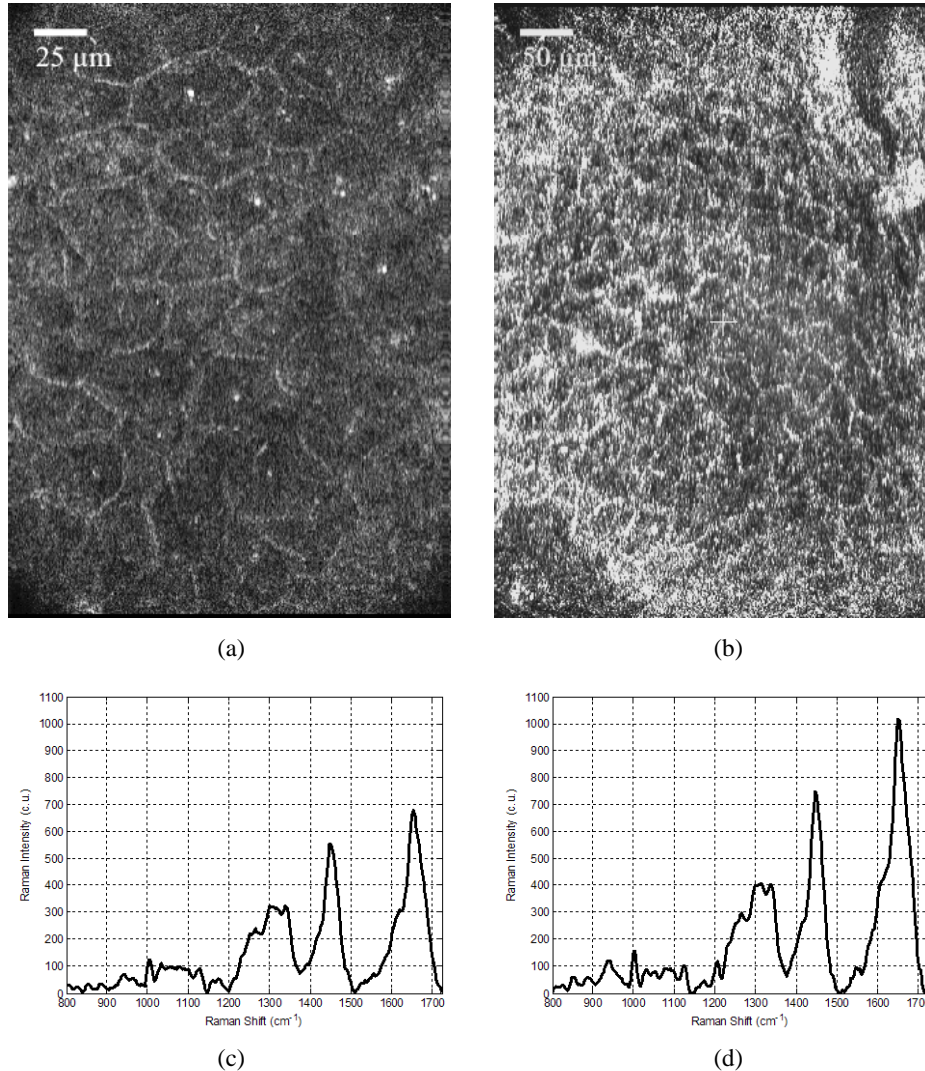
| (a) | (b) |

| (c) | (d) |

Fig. 6. Images and spectra acquired from the fingertip using the 100x objective and hemisphere (a,c) and 50x objective and hemisphere (b,d). Cell membranes and nuclei are easily distinguished in (a), but nuclear detail is less evident when using the lower magnification objective (b). Image size is 260 x 198 µm and 520 x 396 µm for (a) and (b) respectively. Corresponding Raman spectra demonstrate the fact that the 50x objective allows for greater detected Raman signal intensity.

autofluorescence [15]. The plots depict the un-normalized Raman scattering intensity after fluorescence subtraction in order to demonstrate the relative difference in overall performance between the 100x objective and the 50x objective.

4.2. Axial and transverse sectioning potential in the skin

Co-registered images and spectra were acquired from different tissue features in the skin that were closely separated in the axial and transverse planes in order to demonstrate the sectioning capabilities of the handheld CM-CRS microscope. Figure 7 shows the CM – CRS data acquired from the volar forearm, at a depth of approximately 120 μm, in and around a
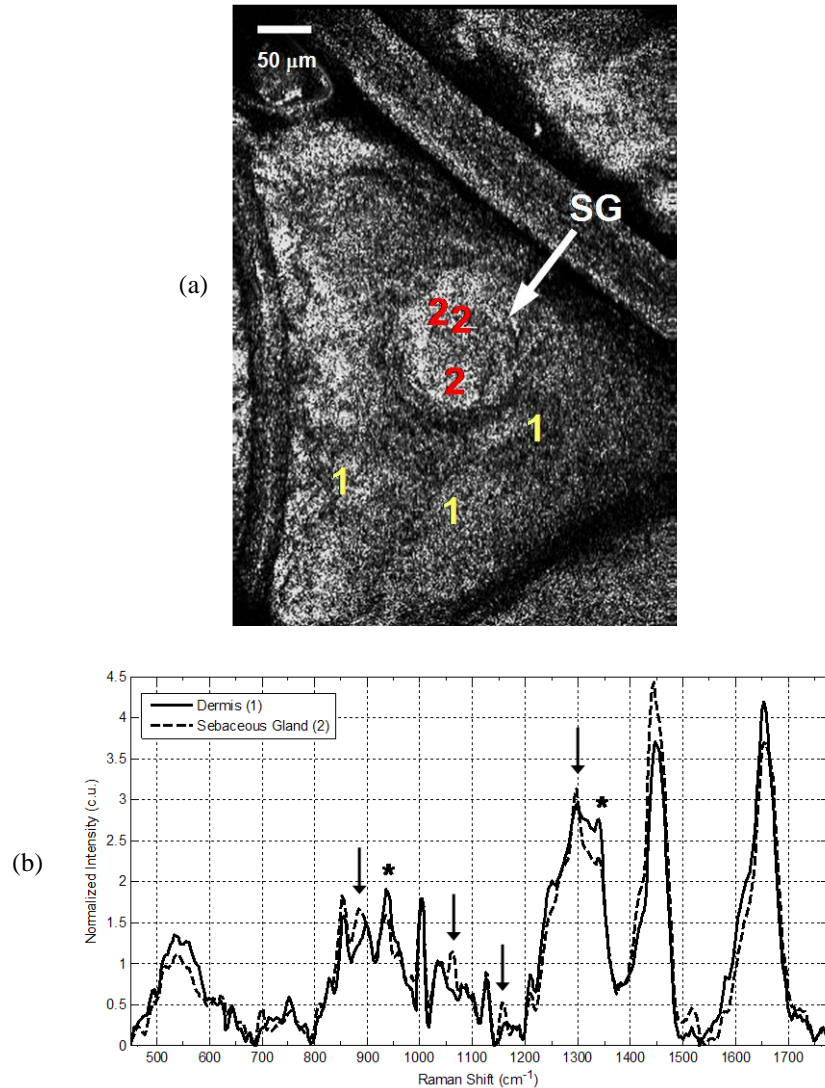

Fig. 7. *In vivo* CM image and CRS spectra of a sebaceous gland and the adjacent skin taken with 50x objective. (a) CM image shows the presence of the large circular sebaceous gland (SG) in the center of the image, and indicates the positions from which spectra were acquired (+)(Red-Dermis, Purple-Sebaceous). (b) Mean spectra acquired from within the sebaceous gland (purple line) and from the adjacent dermis (red line). Spectral features characteristic of the fatty acids within sebum are seen at 884,, 1062, 1157 cm^{-1}, and 1297 cm^{-1} (arrows), while typical tissue protein features (*) such as those at 936 and 1339 cm^{-1} are more prevalent in the adjacent skin.
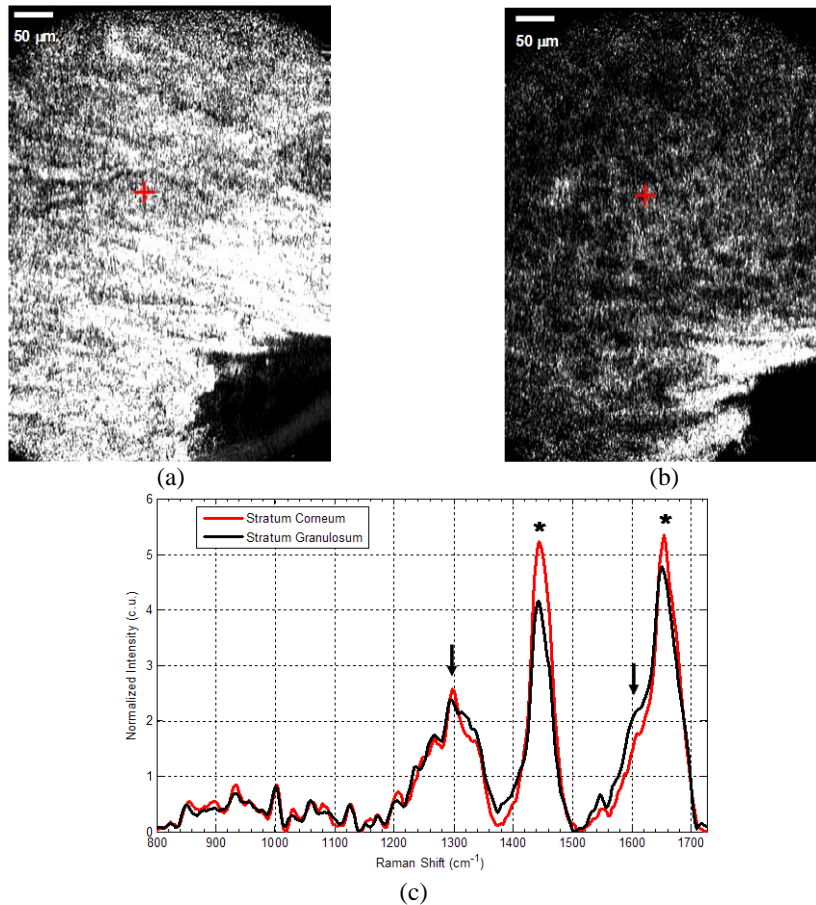
(a)

(b)

(c)

Fig. 8. CM and CRS from normal stratum corneum (SC) and stratum granulosum (SG) on the cheek of a Caucasian male. SC image (a) shows the bright polygonal corneocytes distinguished by the dark regions separating them. The SG image (b), acquired just 20 μm below the (a), shows distinctly different round epidermal cells with the hyporeflective cell soma and bright membranes. The corresponding CRS spectra (c), show differences in the spectral lineshape around 1300 cm^{-1} and 1600 cm^{-1} (arrows), and in the relative intensities of the CH$_x$ peak at 1440 cm^{-1} and the amide I band at 1650 cm^{-1} (*). Spectral features characteristic of the SC, including the sharp lipid peak at 1297 cm^{-1}, while the SG is characterized by increased spectral intensity at the amide I shoulder at 1600 cm^{-1}, and the increased relative intensity of the amide I peak.

sebaceous gland. In the CM images (Fig. 7 (a)), the sebaceous gland is seen as the large round feature in the middle of the image. Raman spectra were then acquired at the positions indicated in Fig. 7 (a). Spectral acquisition time was 30 seconds for all measurements. The tissue auto-fluorescence was subtracted and the spectra were then area normalized for direct comparison. The mean of the three spectra acquired from each region can be seen in Fig. 7 (b). Differences between the spectra occur in the 500 – 600 cm^{-1} band, and at 884, 940, 1062, 1157 cm^{-1}. There is a difference between the two spectra's line-shape in the band from 1250 to 1350 cm^{-1}, as well as differences between the relative intensities of the peaks at 1440 and 1650 cm^{-1}.

Figure. 8 shows a set of images and spectra acquired from adjacent layers of the skin; the stratum corneum (SC), and the stratum granulosum (SG). The CM image of the SC (Fig. 8 (a)) is characterized by marked hyper-reflectivity and the presence of large, polygonal shaped cells that do not contain visible nuclei. A set of 3 Raman spectra were acquired from

the plane imaged in Fig. 8 (a), and the objective was then translated approximately 20 microns deeper into the tissue where a 2nd set of images and spectra were acquired. The CM image in Fig. 8 (b) is noticeably different from that acquired in the SC. The image depicts a layer of round cells with distinct cell membranes and dark, hypo-reflective cell somas. Figure 8 (c) reflects the mean spectra acquired from the SC and SG. Here, there are noticeable differences in the spectral line-shape around 1300 cm^{-1} and 1600 cm^{-1}, and in the relative intensities of the 1440 and 1650 cm^{-1} peaks. All measurements were taken with the 50x objective and hemisphere front piece, with CRS acquisition times of 30 seconds.

5. Discussion

We report the successful combination of CM and CRS into a handheld probe for dual-modal imaging and spectroscopy. The overall size of the sampling probe, which can typically be the size of a benchtop microscope, has been reduced to 7" (L) x 4.5" (W) x 2.25" (H). The reduction in size is due to a design that incorporates a MEMS mirror for raster scanning the CM laser beam. In addition, the distal location of all of the instrument's control and detection hardware keeps the equipment remotely stored from the microscope. The reduced size allows the probe to be handheld (Fig. 1 (b)) and thus positioned in a number of different orientations beyond the standard upright orientation of benchtop microscopes. The flexibility of the handpiece affords the ability to make measurements of the skin across the body, as is demonstrated by the data acquired from the cheek of a volunteer in Fig. 8. It should be noted that fine positioning and stability of the probe does require skill and dexterity. Our early experience indicates applying firm pressure with the probe towards the skin's surface can produce sufficient stability to perform well registered measurements on the scale of a few cells (≈20 μm). The operator can use the stability of the CM images to ensure that the probe positioning is sufficient to perform accurate measurements. Although the handheld design and small physical footprint of the instrument do give the operator the flexibility to position the probe in a simple and adaptable manner, some circumstances may benefit from additional mechanical stabilization, such as with a mounting arm. These issues are representative of the challenges to be addressed when moving forward with further *in vivo* measurements, but are likely to have less of an impact in other applications where the sample is inanimate, such as forensics, anthropology, or materials science.

The design of the microscope allows for the use of interchangeable objective lenses to make measurements that are either optimized for FOV or resolution. The CRS sub-system was tested with collection fibers with different core sizes to explore the relationship between spatial resolution and SNR, and we arrived at a compromise configuration based on the intended application in the skin. The instrument also incorporates a hemisphere aperture interface with the sample that expands the NA by a factor of 1.5 and improves both image quality and spectral SNR. The performance was demonstrated through the acquisition of images and spectra in the skin that demonstrate the ability to resolve both the structural and biochemical characteristics of small features and thin layers within the skin.

An important decision with respect to the CRS subsystem design was the selection of an appropriate detection fiber size. Although a smaller detection aperture for CRS does improve resolution, the instrument's application for tissue measurements dictates that the implications of optimizing for resolution must be carefully considered. In a clinical setting, the ability to acquire a high quality spectrum in 30 seconds or less is an important performance target. Longer acquisition time can often result in motion artifact, unease for the patient, and generally reduces the practicality of the instrument. Although the best axial resolution (10 μm) was achieved with the 8 μm CRS detection fiber, the improved axial sectioning capacity in comparison to the 50 μm detection fiber (17.6 μm resolution) was not determined to be worth the > 5 decrease in SNR. In addition, our testing determined it was not possible to get quality spectral measurements from tissue using the 8 μm detection fiber within 30 seconds, while it was possible with the 50 μm fiber. As a result, all the CRS data collected from the skin in this manuscript was collected with a 50 μm CRS detection fiber. The broadened tails seen in Fig. 3(b) are the result of this decision to use a larger, multimode fiber for CRS

detection. The final design is driven by the challenges of acquiring *in vivo* tissue measurements. For applications where stable samples would permit slightly longer acquisition times, improved resolution could be achieved.

Previous work has demonstrated that improved CM imaging performance can be achieved by expanding the microscope's NA with a glass hemisphere front-piece [11]. The hemisphere's curvature is designed to match the wavefront of the converging beam, and thus increase the magnification and NA. The NA of the 50x objective can thus be increased from 0.55 to 0.83, while the NA of the 100x can be increased from 0.75 to 1.13. In the course of evaluating the tradeoff between CRS resolution and SNR as a function of detection fiber size, it became clear that the increase in magnification and NA due to the hemisphere front piece also improves the CRS performance. The glass hemisphere also provides an excellent surface to locally stabilize the subject's skin during measurement sessions, which reduces motion artifact and allows for greater reproducibility in the measurements. The quantitative benefit of the hemisphere front-piece with respect to both CM and CRS resolution and CRS SNR combined with its ability to stabilize the sample and simplify superficial targeting make it an essential feature for future *in vivo* applications.

Since the skin is a complex tissue with features that span a wide range of length scales from a few microns up to a few centimeters, it is important that the microscope be designed to accommodate to the specific features of interest as much as possible. Although the microscopic nature of CM fundamentally limits the FOV achievable with a single image, the flexibility to interchange objectives based on the specific application can be a useful feature. The 100x objective has sufficient magnification to image detailed cellular features such as nuclei quite clearly, while identifying nuclei with the 50x objective is more difficult. The benefit of the 50x objective, however, is that it has twice the FOV. With respect to the CRS subsystem, the 100x objective we used is not NIR optimized, and does not have as high a throughput from 785 nm to 1000 nm as the 50x objective. This reduces the intensity of both the delivered and collected light. In addition, the illumination beam is designed to fill the 3.0 mm back aperture of the 100x objective in order to achieve the best possible imaging resolution. The 50x objective, on the other hand, has a 4.3 mm back aperture, and thus allows for a slightly larger percentage of the overall beam energy to pass through the lens. Ultimately, the larger back aperture and IR optimized optics facilitate more efficient CRS with the 50x objective, although this benefit comes at the expense of CM imaging resolution.

Figure. 7 demonstrates an example in which the instrument is capable of probing biochemical differences between microstructures that exist in close transverse proximity to one another. In this instance the sebaceous structure appears as a large round feature in the center of the image. The single-micron scale transverse resolution CM imaging enables the general morphology of the gland to be visualized and targeted for biochemical characterization with RS. Comparison of the mean spectra acquired within the gland and immediately adjacent to the gland reveals spectral differences that provide valuable compositional information and confirm the structure is a sebaceous gland. The distinct presence of peaks at 884, 1062, and 1157 cm^{-1}, and the sharp line-shape of the peak at 1297 cm^{-1}, are characteristic of the type of fatty acids that make up the sebum and are consistent with previously reported CRS measurements of sebaceous glands [16]. The mean spectrum collected from the adjacent skin,, does not show features characteristic of sebum or fatty acids, and instead contains spectral features more characteristic of cellular proteins, based on the relative intensity of spectral bands at 936 cm^{-1} and 1339 cm^{-1} [17]. This example illustrates the benefit of a dual-modal approach that utilizes image guidance and targeting to improve the spatial specificity of CRS. The ability to visualize the general morphology of the cells and structures in a region of interest and target specific sub-surface microscopic structures with CRS can be critical in diagnosing diseased skin lesions such as tumor cell nests or identifying specific glands or structures in basic skin research. Nevertheless, identification of the subtle differences between Raman spectra will also require application of robust statistical analysis techniques, including feature extraction and pattern recognition [18] to achieve the best results.

In addition to transverse targeting, the high-resolution axial sectioning ability of the microscope allows localization of spectral measurements at various depths, as demonstrated in Fig. 8. Here, the images and spectra are acquired from two different layers of the skin only 20 μm apart. The SC is the topmost layer of the epidermis and is made up of large anuclear, polygonal corneocytes that are filled with keratin and appear hyper-reflective and bright (Fig. 8 (a)). The corneocytes are separated by waxy lipids that are important in maintaining the hydration of the lower epidermal layers and can be seen as the dark boundaries between individual corneocytes [19]. Slightly below the SC is the SG, which contains epidermal cells that have lost their nuclei but are still producing keratin and lipids, and retain a rounder shape. These features are evident in Fig. 8 (b) and are dramatically different in appearance in comparison to the SC image (Fig. 8 (a)). The corresponding CRS spectra (Fig. 8 (c)) show features indicative of the biochemical differences between the SC and the SG as well. The SC spectrum has a line-shape that is characteristic of that previously attributed to the SC [13], including the 1297 cm^{-1} peak line-shape, and relatively equal intensities of the 1440 cm^{-1} CH$_x$ peak and the 1660 cm^{-1} amide I peaks. The SG spectrum, on the other hand, does not contain these features, and instead has a spectral line-shape with more muted lipid features, and increased spectral intensity in specific protein bands, such as the shoulder of the amide I peak at 1600 cm^{-1} [13]. Because of the inherent micro-anatomical variation in layer thickness both within patients and across the population, collection of spectra from specific layers cannot be performed by simply acquiring measurements from a specific depth below the skin's surface. If the experimental objective is to target a specific layer of interest using CRS alone, it can be a painstaking and difficult task that requires acquisition of spectral profiles consisting of many measurements spaced microns apart in depth, and subsequent analysis of spectral features corresponding to certain layers. Here the collected spectra and images correlate well with the known features of the SC and SG, and demonstrate the ability of a dual-modal CM-CRS device to simplify acquisition of spectra from specific layers within the epidermis. The maximum depth at which correlated CRS and CM data can be acquired is largely dependent on the optical properties of the sample, which can vary substantially. In the skin, this variability can be particularly high due to differences in pigmentation, skin type, age, and location on the body. However, in our experience, correlated measurements can be made through the epidermis at depths of up to 200 μm on the back of the hand of a lightly pigmented Caucasian. Although increasing the incident laser power at the skin's surface beyond the 50 W/cm^2 used to acquire the data in Figs. 8 (b,c) would increase the imaging depth, it is likely unnecessary. Prior studies in both CM and CRS have shown the ability to acquire diagnostically relevant data within the epidermis at even shallower depths while showing no signs of tissue damage [18,20].

It is important to note that the benefits of a CM-CRS system are mutual, and extend beyond the ability of CM to guide CRS. Contrast in CM images arises simply from the reflectivity of the sample, and there is no intrinsic source of data that can directly relate molecular composition. In the case of clinical diagnostics, CM images are quite comparable to histology sections in terms of structure; however they do not exhibit the specific contrast that various tissue stains provide in conventional pathological diagnosis. The instrument we report has the ability to characterize the biochemical composition of specific features within the CM field, and although this is not analogous to adding true molecular contrast to the CM images, it does complement the structural sensitivity of CM with biochemically specific CRS measurements.

6. Conclusion

We have reported the development of a handheld CM-CRS microscope capable of high-resolution imaging spectroscopy outside of the typical benchtop-microscope setting. The handheld unit utilizes a MEMS scanning mirror to achieve a compact design, while remote positioning of the light source, detection systems, electronics, and instrument controls minimizes the size of the probe. We have characterized the performance of the probe with respect to axial and transverse resolution, CRS detection fiber size, and CM-CRS co-

registration. The instrument is capable of achieving an imaging resolution of up to 1.5 μm (axial) x 0.4 μm (transverse), and a spectroscopic resolution of up to 13 μm (axial) x 0.79 μm (transverse). The tradeoff between axial resolution and SNR as a function of CRS detection fiber size resulted in the use of a 50 μm detection fiber based on the desired application to *in vivo* analysis of the skin. Co-registration of CRS and CM was verified to within 5 μm. The performance of the probe was then demonstrated by performing *in vivo* measurements from different layers of the skin, including the stratum corneum, stratum granulosum, and dermis as well as micro-structures such as sebaceous glands, with confocal reflectance imaging while providing chemical differences of tissue through Raman spectroscopy. The combined system can provide beneficial data collection for diagnostic purposes.

Acknowledgments